Nonlinear Multiscale Wavelet Diffusion for Speckle Suppression and Edge Enhancement in Ultrasound Images

Yong Yue, *Student Member, IEEE*, Mihai M. Croitoru, Akhil Bidani, Joseph B. Zwischenberger, and John W. Clark, Jr., *Fellow, IEEE*

Abstract—This paper introduces a novel nonlinear multiscale wavelet diffusion method for ultrasound speckle suppression and edge enhancement. This method is designed to utilize the favorable denoising properties of two frequently used techniques: the sparsity and multiresolution properties of the wavelet, and the iterative edge enhancement feature of nonlinear diffusion. With fully exploited knowledge of speckle image models, the edges of images are detected using normalized wavelet modulus. Relying on this feature, both the envelope-detected speckle image and the log-compressed ultrasonic image can be directly processed by the algorithm without need for additional preprocessing. Speckle is suppressed by employing the iterative multiscale diffusion on the wavelet coefficients. With a tuning diffusion threshold strategy, the proposed method can improve the image quality for both visualization and auto-segmentation applications. We validate our method using synthetic speckle images and real ultrasonic images. Performance improvement over other despeckling filters is quantified in terms of noise suppression and edge preservation indices.

Index Terms—Dyadic wavelet transform, iterative denoising, multiscale analysis, nonlinear diffusion, speckle suppression, ultrasound imaging, wavelet diffusion.

I. INTRODUCTION

ULTRASOUND speckle is the result of the diffuse scattering, which occurs when an ultrasound pulse randomly interferes with the small particles or objects on a scale comparable to the sound wavelength. Speckle is an inherent property of an ultrasound image, and is modeled as spatial correlated multiplicative noise. In most cases, it is considered a contaminating factor that severely degrades image quality.

To improve clinical diagnosis, speckle reduction is generally used for two applications: visualization enhancement and auto-segmentation improvement. Most speckle filters are developed for enhancing visualization of speckle images [1]–[3]. For these approaches, texture recovery is a desired feature of filtering, and needs to be addressed. Another goal of ultrasonic speckle suppression is to improve image simplification, which is in turn very beneficial in automated object detection (e.g., in segmentation and motion tracking). In this sense, texture removal significantly improves the speed and accuracy of automated object detection. Consequently, speckle filters that are designed for texture recovery have rather limited application in auto-segmentation improvement.

We therefore consider the design of a speckle suppression algorithm, which mainly focuses on producing the denoising result for auto-segmentation improvement, but is also able to provide visualization enhancement. For the main goal (segmentation improvement), image texture does not improve boundary tracking. Rather, texture recovery is better ignored. In fact, a simplified image with piecewise smoothing regions and the essential edges of objects, often improves segmentation performance. Such simplification can be described by use of a "cartoon model," which has been elaborated by the Mumford-Shah functional [4].

An image can be simplified using iterative filtering such that the output of each iteration represents a coarser version of its input. A class of techniques for accomplishing that purpose is, the scale-space denoising methods, called nonlinear anisotropic diffusion, e.g., Perona–Malik filter [5], Weickert filter [6] and total variation diffusion [7]. These techniques rely on the diffusion flux to iteratively eliminate small variations due to noise or texture, and to preserve large variations due to edges. For the multiplicative noisy image, however, the general signal/noise relationship no longer exists, since the variations due to noise may be larger than those due to signal. This limits the application of the nonlinear diffusion method in the processing of ultrasound images. A solution is to integrate the speckle suppression algorithm into the diffusion technique. For instance, a speckle reducing anisotropic diffusion (SRAD) method [8] has been derived by casting the typical spatial adaptive filers (the Lee and Frost filter [1], [9]) into the nonlinear diffusion technique. Although the SRAD method improves edge detection via the anisotropic filtering, the filtering result with regard to speckle suppression and edge preservation is still preserved for segmentation purposes. For example, low-contrast edges are often smeared with speckle, and speckle texture is usually retained in the high-intensity region.

The nonlinear diffusion technique relies on the gradient operator to distinguish signal from noise. Such a method often cannot achieve a precise separation of signal and noise. Ultrasound image denoising problems are better solved if a powerful

Y. Yue is with Department of Electrical and Computer Engineering, Rice University, Houston, TX 77005 USA (e-mail: yyue@rice.edu).

M. M. Croitoru and A. Bidani are with University of Texas Medical School at Houston, Houston TX 77030 USA.

J. B. Zwischenberger is with University of Texas Medical Branch, Galveston, TX 77555 USA.

*J. W. Clark, Jr. is with Department of Electrical and Computer Engineering, Rice University, Houston, TX 77005 USA (e-mail: jwc@rice.edu).

signal/noise separating tool (e.g., wavelet analysis) is incorporated in the speckle-reducing diffusion process. Moreover, multiscale wavelet despeckling methods have demonstrated tremendous performance improvement compared to typical spatial speckle filters [10]–[12]. Intuitively, integration of the multiresolution and sparsity properties of the wavelet with anisotropic speckle reduction from nonlinear diffusion should lead to stronger speckle suppression and edge preservation than that achieved by spatial domain filtering alone. Recent work [13] has shown that nonlinear anisotropic diffusion can be employed within framework of the dyadic wavelet transform (DWT). We refer to the integration of nonlinear diffusion and wavelet shrinkage as *wavelet diffusion*. Inherited from the wavelet, this technique has more favorable denoising properties than nonlinear diffusion (namely, via multiscale analysis and more efficient signal/noise separation). It is also distinguished from wavelet-based denoising methods by its improved edge-enhancement and iterative noise reduction features.

In this paper, we present a normalized modulus-based nonlinear multiscale wavelet diffusion (NMWD) method for speckle suppression and edge enhancement. The proposed approach aims to improve the ultrasound image quality for automated image interpretation. With a tunable parameter, the algorithm can also preserve texture for visual enhancement. The proposed algorithm is versatile for both the envelope-detected speckle image and the log-compressed ultrasonic image. Relying on edge detection by the normalized wavelet modulus, the algorithm can directly take either type of image as input without prior compressing via the logarithmic transform or uncompressing via the exponential function. This feature actually solves the performance instability problem, which is caused by inaccurate estimation of the compression coefficiente—a tricky problem for most speckle filters.

The paper is organized as follows. In Section II, we review the theories of nonlinear diffusion, the dyadic wavelet transform and two–dimensional (2-D) wavelet diffusion. In Section III, we introduce the new algorithm. In Section IV, we quantify the performance of our algorithm and present results for both synthetic (simulated) and real ultrasonic images. Conclusions are drawn in Section V.

II. WAVELET DIFFUSION

A. Nonlinear Diffusion

Perona and Malik proposed a fundamental nonlinear anisotropic diffusion based on partial differential equation (PDE) for noise smoothing [5], [6]. Given a noisy image $f(x, y, t)$ at time (scale) t, the nonlinear diffusion equation is expressed as

$$\begin{cases} \frac{\partial}{\partial t} f(x, y, t) = div\left[c(x, y, t)\nabla f(x, y, t)\right] \\ f(x, y, 0) = f_0(x, y) \end{cases} \quad (1)$$

where ∇ is the gradient operator, div is the divergence operator, and $c(x, y, t)$ is the diffusion coefficient. If $c(x, y, t)$ is a constant, (1) reduces to the isotropic heat diffusion equation. To avoid the edge-smearing during the diffusion, $c(x, y, t)$ should be constructed to encourage homogenous-region smoothing and to inhibit the smoothing across the boundaries. A satisfied $c(x, y, t)$ is determined by two components: the edge map $\eta(x, y, t)$ and the diffusivity function $g(\cdot)$. The edge map

$\eta(x, y, t)$ is the estimation of the location of the edges at time t. Ideally, $\eta(x, y, t)$ should have the following two properties:

1) $\eta(x, y, t)$ equals to zero for the region inside boundaries;
2) $\eta(x, y, t)$ has the local contrast at edge point in a direction perpendicular to the edge.

In the scale space, $\eta(x, y, t) = \nabla f(x, y, t)$ can generally provide an accurate estimation of the edge positions. The diffusivity function $g(\cdot)$ has to be a nonnegative monotonically decreasing function, with $g(0) = 1$. As a consequence, $c(x, y, t)$ can be formulated as

$$c = g\left(|\eta|\right). \quad (2)$$

A diffusivity function proposed in [5] is given by

$$g\left(|\eta|\right) = \frac{1}{1 + \left(\frac{|\eta|}{\lambda}\right)^2} \quad (3)$$

where λ is an edge magnitude threshold parameter. The influence of λ on the diffusion process can be illustrated by the flux, defined as $\Phi(\eta) = g(\eta)\eta$ [5]. Given a value of λ, the maximum flux Φ_M occurs at $|\eta| = \lambda$ for (3) [14]. Below Φ_M, the flux is reduced to zero, indicating that diffusion encourages homogenous region smoothing. Above Φ_M, the flux also goes to zero, suggesting that diffusion inhibits smoothing across edges. Generally, a large value of λ produces a smoother result in a homogenous region than a smaller one. In this sense, λ acts as a threshold for the diffusion process.

B. Dyadic Wavelet Transform

Mallat and Zhong [15] have generalized the Canny edge detection approach, and have presented a multiscale dyadic wavelet transform for the characterization of one—dimensional (1-D) and 2-D signals. With a wavelet function $\psi(x) \in L^2(R)$, a continuous wavelet transform of $f(x)$ is given by

$$W_{a,b}f(x) = \langle f, \psi_{a,b} \rangle = \int_{-\infty}^{+\infty} f(x)\frac{1}{a}\psi\left(\frac{x - b}{a}\right) dx \quad (4)$$

where $a > 0$ is the scale number, $b \in R$ is the translation parameter, and $\psi_{a,b}(x) = (1/a)\psi(x - b/a)$. With a differentiable smoothing function $\theta(x)$, $\psi(x)$ is given by

$$\psi(x) = \frac{\partial \theta(x)}{\partial x}.$$

For the 2-D wavelet transform, the wavelet functions $\psi^1(x, y)$ and $\psi^2(x, y)$ are defined as

$$\psi^1(x, y) = \frac{\partial \theta(x, y)}{\partial x} \text{ and } \psi^2(x, y) = \frac{\partial \theta(x, y)}{\partial y}. \quad (5)$$

The dyadic wavelet transform of $f(x, y) \in L^2(R^2)$ at the scale 2^j (or level j) has two components defined by

$$W_j^d f(x, y) = f * \psi_j^d(x, y) \quad d = 1, 2. \quad (6)$$

Hence, the wavelet coefficients $W_j^1 f(x, y)$ and $W_j^2 f(x, y)$ are proportional to the gradient of $f * \theta(x, y)$

$$\begin{pmatrix} W_j^1 f(x, y) \\ W_j^2 f(x, y) \end{pmatrix} = 2^j \begin{pmatrix} \frac{\partial}{\partial x}(f * \theta_j)(x, y) \\ \frac{\partial}{\partial y}(f * \theta_j)(x, y) \end{pmatrix}$$

$$= 2^j \nabla(f * \theta_j)(x, y). \quad (7)$$

The modulus of the wavelet coefficients at scale 2^j is defined as

$$M_j f(x, y) = \sqrt{\left|W_j^1 f(x, y)\right|^2 + \left|W_j^2 f(x, y)\right|^2} \quad (8)$$

which represents the multiscale edge information obtained by combining the horizontal and vertical wavelet coefficients. With a scaling function $\phi(x, y)$, the coarse approximation of $f(x, y)$ at scale 2^j is

$$S_j f(x, y) = f * \phi_j(x, y). \tag{9}$$

A finite-level discrete dyadic wavelet transform of the 2-D discrete function $f \in l^2(Z^2)$ can be represented as

$$W = \left\{ S_J f, \left(W_j^d f \right)_{1 \leq j \leq J}^{d=1,2} \right\} \tag{10}$$

where $S_J f$ is a coarse scale approximation of f at final scale 2^J, and $W_j^d f$ represents the detail image at scale 2^j. We refer to this discrete wavelet transform as the MZ-DWT.

A 2-D discrete function f can be decomposed by a lowpass filter H and a highpass filter G, and reconstructed with a lowpass filter $\tilde{H}$ (the conjugate filter of H) and two highpass filters K and L. In the Fourier domain, the Fourier transform of five filters are denoted by $\hat{H}$, $\hat{G}$, $\hat{\tilde{H}}$, $\hat{K}$ and $\hat{L}$, respectively. Details about filter construction can be found in [15] and [13]. The coarse scale approximation of $f(u, v)$ at scale 2^{j+1} can be represented in the Fourier domain as

$$\hat{S}_{j+1} f(u, v) = \hat{H}(2^j u) \hat{H}(2^j v) \hat{S}_j f(u, v) \tag{11}$$

where $j \geq 0$, and $\hat{S}_0 f(u, v) = \hat{f}(u, v)$. Correspondingly, the two detail images are obtained as

$$\hat{W}_{j+1}^1 f(u, v) = \hat{G}(2^j u) \hat{S}_j f(u, v) \tag{12}$$
$$\hat{W}_{j+1}^2 f(u, v) = \hat{G}(2^j v) \hat{S}_j f(u, v). \tag{13}$$

With the reconstruction filters, the signal is represented recursively as

$$\begin{aligned} \hat{S}_j f(u, v) = & \hat{S}_{j+1} f(u, v) \hat{\tilde{H}}(2^j u) \hat{\tilde{H}}(2^j v) \\ & + \hat{W}_{j+1}^1 f(u, v) \hat{K}(2^j u) \hat{L}(2^j v) \\ & + \hat{W}_{j+1}^2 f(u, v) \hat{L}(2^j u) \hat{K}(2^j v). \end{aligned} \tag{14}$$

The time domain representation of (11)–(14) can be found in [13], [15]. By substituting (11)–(13) into (14), a necessary and sufficient condition for perfect reconstruction is given as [16]:

$$\hat{\tilde{H}}(u) \hat{\tilde{H}}(v) \hat{H}(u) \hat{H}(v) + \hat{K}(u) \hat{L}(v) \hat{G}(u) + \hat{L}(u) \hat{K}(v) \hat{G}(v) = 1. \tag{15}$$

C. Wavelet Diffusion

Recently, Mrázek *et al.* [17] have sought to determine the correspondence between wavelet shrinkage and nonlinear diffusion methods. Shih *et al.* [13] have shown that nonlinear diffusion can be approximated by a MZ-DWT shrinkage process, and have proposed a novel denoising scheme which combines the two techniques. We refer to the integration of nonlinear diffusion and wavelet shrinkage as *wavelet diffusion*. This integrated technique has several favorable denoising properties inherited from the individual techniques (e.g., multiscale analysis and efficient signal/noise separation properties from the wavelet, edge-enhancement and iterative noise reduction features from the nonlinear diffusion). A derivation that proceeds from 1-D nonlinear diffusion to dyadic wavelet shrinkage has

been shown in [13]. For our application, we briefly demonstrate the derivation in 2-D. From (1), we have

$$\begin{aligned} \frac{\partial}{\partial t} f(x, y, t) = & \frac{\partial}{\partial x} \left[c(x, y, t) \frac{\partial}{\partial x} f(x, y, t) \right] \\ & + \frac{\partial}{\partial y} \left[c(x, y, t) \frac{\partial}{\partial y} f(x, y, t) \right]. \end{aligned} \tag{16}$$

Forward time discretization of the time derivative is approximated as

$$\frac{\partial}{\partial t} f(x, y, t) = \frac{f(x, y, t + \triangle t) - f(x, y, t)}{\triangle t} + O(\triangle t).$$

Neglecting the higher-order terms, and substituting the above equation into (16), we obtain

$$\begin{aligned} \frac{f(x, y, t + \triangle t) - f(x, y, t)}{\triangle t} = & \frac{\partial}{\partial x} \left[c(x, y, t) \frac{\partial f(x, y, t)}{\partial x} \right] \\ & + \frac{\partial}{\partial y} \left[c(x, y, t) \frac{\partial f(x, y, t)}{\partial y} \right]. \end{aligned} \tag{17}$$

With $\triangle t = 1$, we can approximate (17) as

$$\begin{aligned} f(x, y, t + 1) \approx & f(x, y, t) + \frac{d}{dx} \left[c(x, y, t) \frac{df(x, y, t)}{dx} \right] \\ & + \frac{d}{dy} \left[c(x, y, t) \frac{df(x, y, t)}{dy} \right] \end{aligned} \tag{18}$$

and denote $f(x, y, t + 1)$, $f(x, y, t)$ and $c(x, y, t)$ as $\tilde{f}(x, y)$, $f(x, y)$ and $c(x, y)$, respectively, for briefness. Letting $p(x, y) = 1 - c(x, y)$, (18) can be rewritten as

$$\begin{aligned} \tilde{f}(x, y) = & f(x, y) + \frac{d^2 f(x, y)}{dx^2} + \frac{d^2 f(x, y)}{dy^2} \\ & - \frac{d}{dx} \left[p(x, y) \frac{df(x, y)}{dx} \right] - \frac{d}{dy} \left[p(x, y) \frac{df(x, y)}{dy} \right]. \end{aligned} \tag{19}$$

The Fourier transform of (19) is

$$\begin{aligned} \hat{\tilde{f}}(u, v) = & (1 - u^2 - v^2) \hat{f}(u, v) - ju \left[\frac{1}{2\pi} \hat{p}(u, v) * \left(ju \hat{f}(u, v) \right) \right] \\ & - jv \left[\frac{1}{2\pi} \hat{p}(u, v) * \left(jv \hat{f}(u, v) \right) \right]. \end{aligned} \tag{20}$$

Letting $\hat{A}_1 \cdot \hat{A}_2 = 1 - u^2 - v^2$; $\hat{B} = ju$; $\hat{D} = -ju$; $\hat{E} = jv$; $\hat{F} = -jv$ and $\hat{p} = (1/2\pi) p(u, v)$, and substituting into (20), we have

$$\begin{aligned} \hat{\tilde{f}}(u, v) = & \hat{A}_2 \cdot \hat{A}_1 \cdot \hat{f}(u, v) + \hat{D} \cdot \left(\hat{p} * \left(\hat{B} \cdot \hat{f}(u, v) \right) \right) \\ & + \hat{F} \cdot \left(\hat{p} * \left(\hat{E} \cdot \hat{f}(u, v) \right) \right). \end{aligned} \tag{21}$$

We note that (21) has the same format as (14). In addition

$$\hat{A}_1 \cdot \hat{A}_2 + \hat{B} \cdot \hat{D} + \hat{E} \cdot \hat{F} = 1$$

which satisfies the filter requirement expressed in (15). Finally, the inverse Fourier transform of (21) is

$$\begin{aligned} \tilde{f}(x, y) = & (f(x, y) * A_1) * A_2 + (p(x, y) \cdot (f(x, y) * B)) * D \\ & + (p(x, y) \cdot (f(x, y) * E)) * F. \end{aligned} \tag{22}$$

Equation (22) indicates that the image $f(x, y)$ is first decomposed with the lowpass filter A_1 and the highpass filters B and E. It is then regularized with $p(x, y)$, and finally reconstructed
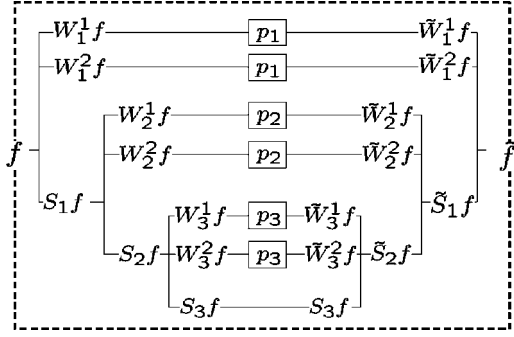
Fig. 1. Scheme for 3-level wavelet diffusion. $\bar{S}_j f$ and $\bar{W}_j^d f$ denote the filtered wavelet coefficients at scale 2^j.

with the corresponding lowpass filter A_2 and the highpass filters D and F.

From the derivation (see (19)), the diffusion coefficient $c(\cdot)$ has its correspondence with $p(\cdot)$ in the wavelet domain. Similar to $c(\cdot)$ in (1), the diffusion behavior of $p(\cdot)$ is also determined by the edge map η and the diffusivity function $g(\cdot)$. Therefore, *wavelet diffusion coefficient* is given by

$$p\left(|\eta|\right) \equiv 1 - g\left(|\eta|\right). \tag{23}$$

To achieve edge-preservation and intra-region smoothing, $g(\cdot)$ in (23) also has to be a nonnegative monotonically decreasing function. In this sense, most diffusivity functions [18], which have already been developed in the nonlinear diffusion, can be used in wavelet diffusion. Another important factor controlling the effect of the diffusion is the selection of the edge map η. For a general denoising problem (e.g., additive Gaussian noise), either wavelet coefficients or wavelet modulus can be used as the edge map. However, from (7), the similarity of the gradient operator and the wavelet modulus suggests that the wavelet modulus may be more appropriate.

The advantages of wavelet-based diffusion over spatial non-linear diffusion are obvious: the edges detected by the wavelet coefficients/modulus are more accurate than the ones estimated by the gradient operator. Moreover, multiscale analysis provides powerful denoising scheme for the treatment of complicated noise, including speckle. Similar to the wavelet shrinkage [19], the denoising scheme of wavelet diffusion is implemented by three steps: 1) the noisy image f is decomposed into the coarse scale approximation $S_j f$ ($j \geq 1$) and detail images $W_j^d f$ ($d = 1, 2$) by 2-D MZ-DWT; 2) wavelet coefficients $W_1^d f$ are regularized as

$$\tilde{W}_j^d f = p\left(|\eta|\right) W_j^d f. \tag{24}$$

3) the denoised image is reconstructed by taking the inverse MZ-DWT. To achieve a satisfactory denoising result, wavelet diffusion is often performed iteratively [13]. For instance, a three-level wavelet diffusion scheme is shown in Fig. 1.

III. Speckle Suppression With Wavelet Diffusion

Wavelet diffusion can be considered as a special case of non-linear diffusion which is employed within the framework of the dyadic wavelet transform. In denoising applications, the key issue of wavelet diffusion is to find an accurate edge estimation method. For the image corrupted with additive Gaussian noise,

wavelet coefficients (or wavelet modulus) can precisely distinguish the edge-related components from noise-related components relying on the difference of their magnitude. However, when an image is contaminated with multiplicative noise, use of the wavelet coefficient as an edge estimator experiences difficulty in efficiently detecting edges, since the noise-related components may indeed be larger than the edge-related components [20]. A similar problem occurs when the nonlinear diffusion technique is employed in speckle suppression. For that problem, Yu and Acton [8] proposed a method which cast the spatial adaptive filtering technique into the nonlinear diffusion algorithm. The conceptual similarity between the nonlinear diffusion and wavelet diffusion techniques encourages us to examine their solution more closely at the beginning of this section. Later in this section, we propose our edge-detection scheme and diffusion threshold estimator in the framework of wavelet diffusion.

A. Related Work

As a typical spatial adaptive filter, the Lee filter assumes signal reflectivity r as a stationary random variable, and a linear minimum mean square error estimator is used to eliminate speckle, given by [1]

$$r_s = \mu_s + \left(1 - \frac{C_u^2}{C_s^2}\right)(f_s - \mu_s). \tag{25}$$

Here, μ_s is the mean value of image f for a moving window s, $C_s^2 = \sigma_s^2/\mu_s^2$ is the normalized noisy signal variance, and $C_u^2 = \sigma_u^2/\mu_u^2$ is the normalized noise variance for the homogenous region u.

SRAD is derived by casting the spatial adaptive filter into the variational framework. A SRAD diffusivity function is defined as

$$g(q) = \frac{1}{1 + \frac{\left(q^2 - q_0^2\right)}{\left[q^2\left(1 + q_0^2\right)\right]}} \tag{26}$$

where q is instantaneous coefficient of variation (ICOV), and q_0 is diffusion threshold. The speckle reduction of SRAD can be understood from the relationship of q and q_0 with their correspondence in the spatial adaptive filter. In fact, q in (26) is a variational expression of C_s of (25) in terms of the gradient operator, whereas q_0 is exactly same as C_u [8]. On another hand, the similarity observed between the nonlinear diffusivity function (3) and SRAD diffusivity function (26) indicates the roles of q and q_0 in the speckle diffusion: q plays a role as the speckle edge detector in the same manner as the edge detector η in nonlinear diffusion, whereas q_0 acts as the diffusion threshold λ. The conceptual correspondence of different denoising techniques is illustrated in Table I.

In the spatial nonlinear diffusion scheme, the solution proposed by SRAD for the despeckling problem is: to estimate the edge map with the normalized noisy signal variance, and to compute the diffusion threshold from the homogenous speckle region. With this strategy, the signal mean is removed during the edge estimation, and the edge-related components can be easily separated from the noise-related components by the magnitude difference. Therefore, it suggests that, the wavelet diffusion can be also successfully employed for speckle suppression as long

	Spatial Adaptive Filter	Nonlinear Diffusion	Wavelet Diffusion
Diffusion coefficient		$c(\cdot)$	$p(\cdot)$
Additive Gaussian noise			
Edge map (η)		∇f	$W_j^d f$ or $M_j f$
Threshold (λ) or noise estimation		Constant or histogram-based estimation [5]	Constant [13]
Multiplicative speckle			
Edge map (η)	C_s	q	$\tilde{M}_j f$
Threshold (λ) or noise estimation	C_u [1]	q_0 [8]	Homogenous region-based estimation

as one can find an appropriate edge detector to represent the intrinsic signal/noise relationship in the wavelet domain, and identify the homogenous speckle region for the diffusion threshold estimation.

B. Edge Detection With Normalized Modulus

Two types of ultrasound images are generally used. One is the envelope-detected speckle image, which can be generated from the recorded RF signals; whereas the other is the displayed ultrasonic image, which is commonly used in medical applications. The latter is generally considered the logarithmic compressed envelope-detected image (e.g., $f_2 = D \ln f_1 + G$, where D is the compression coefficient, and G is the linear gain). This kind of nonlinear compression totally changes the statistics of the envelope-detected signals, and a different compression coefficient also leads to different statistical distribution of signals [21]. To avoid conversion between image types, we propose two different edge detectors corresponding to image type. The advantage of such direct processing is the avoidance of performance instability caused by inaccurate estimation of the compression coefficient.

1) Envelope-Detected Speckle Image: Statistical studies show that envelope-detected signal can be generally represented in terms of a multiplicative noise model [20]

$$f(x) = \mu R(x) n(x) \tag{27}$$

where μ is the average amplitude of the target, and $R(x)$ is the intrinsic signal with mean one, and $n(x)$ is Rayleigh distributed speckle noise with mean one. By definition (4), the wavelet coefficients are [20]

$$W_{a,b} f(x) = \mu \int R(x) n(x) \psi_{a,b}(x) dx. \tag{28}$$

For a homogenous region, $R(x)$ is set to one to analyze the noise contribution, and the wavelet coefficients are proportional to the mean amplitude μ of the signal. Since $n(x)$ has finite energy and $\int_{-\infty}^{+\infty} \psi_{a,b}(x) dx = 0$, the integral of (28) at scale a will be a nonvanishing function of translation b. Therefore, noise contribution to the wavelet coefficients depends on the signal mean.

Generally, the normalized variance on wavelet coefficients $\sigma_{W_j f}/\mu_s$ is used to characterize the intrinsic signal variance [10]. Here, $\mu_s = (\sum_s f)/N$ is the local mean for a window s with N pixels, and $\sigma_{W_j f}^2 = (\sum_s W_j f^2)/N$ is the local variance of the wavelet coefficients. If considering the variance over all

sub-bands, we find that this total variation equals to the variance of modulus, i.e.,

$$\sigma_{M_j f}^2 = \frac{1}{N} \sum_s (M_j f^2) = \frac{1}{N} \sum_s \left(W_j^1 f^2 + W_j^2 f^2 \right).$$

Therefore, the normalized variance on wavelet modulus $\sigma_{M_j f}/\mu_s$ can also characterize the intrinsic signal variation.

Prior to using the normalized modulus as an edge map, two adjustments are made to improve its denoising performance. First, the size of window for the mean estimation is scale-dependent, specifically, $D_j = 2^{j-1}(D_0 - 1) + 1$, where D_0 is original window. Second, noise variance estimation occurs at the current pixel, rather than by local window estimation. Although this adjustment sacrifices the spatial-correlation resistance provided by window estimation, a better edge resolution is achieved. Moreover, the spatial-correlation caused by speckle can be easily solved via the diffusion process. Finally, we propose the following edge detector for the envelope-detected image diffusion:

$$\tilde{M}_j f = \frac{M_j f}{\mu_s}, \quad j = 1, 2, \ldots, J. \tag{29}$$

Using the modulus (rather than the wavelet coefficients) to characterize the noisy signal is well-suited to the purposes of image segmentation. After removal of the signal mean, the edge-related $\tilde{M}_j f$ has a large value, whereas the noise and texture have a small value of modulus. Consequently, an edge-enhanced diffusion process leads to modulus-maximization at edges and piece-wise smoothing within the homogenous regions. Such a result is suitable for the applications of classification and segmentation.

2) Displayed Ultrasonic Image: The medical ultrasonic images (B-Scan images) generated from clinical imaging systems have different properties compared with an envelope-detected image. The signal processing stages contained within the scanner (logarithmic compression, low-pass filtering, interpolation) modify the statistics of the original signal. Experimental measurements [22] show that displayed ultrasonic images can be modeled as

$$f(x) = \mu R(x) + \sqrt{\mu R(x)} n(x) \tag{30}$$

where $n(x)$ is a zero-mean Gaussian noise with mean one. Although this model does not involve logarithmic transformation, it is still referred to as "log-compressed" model by convention. Assuming that a uniform area is scanned (i.e., $R(x) = 1$), it can be easily shown that the mean of log-compressed image is proportional to the variance rather than the standard deviation of the image.
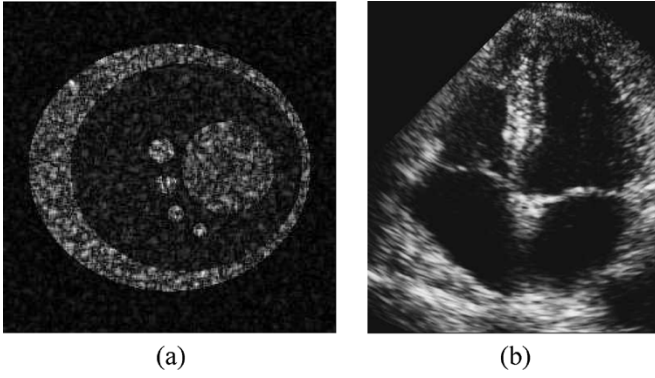
Fig. 2. (a) Simulated envelope-detected speckle image. (b) Real echocardiographic image.

Similar to (28), the wavelet coefficient are given as

$$W_{a,b}f(x) = \mu \int R(x)\psi_{a,b}(x)dx + \sqrt{\mu} \int \sqrt{R(x)}n(x)\psi_{a,b}(x)dx. \quad (31)$$

Considering the noise contribution at homogenous regions $(R(x) = 1)$, we find that the wavelet coefficients are proportional to $\sqrt{\mu}$. To characterize the intrinsic signal/noise variation, the edge detector for the log-compressed ultrasound image is constructed as

$$\tilde{M}_j f = \frac{M_j f}{\sqrt{\mu_s}}, \quad j = 1, 2, \ldots, J. \quad (32)$$

Comparing (29) and (32), the effect of normalization is to remove the signal mean during the edge estimation, and the only difference is the contribution of signal mean to the signal/noise characterization.

3) Statistical Model of Normalized Modulus: The distribution of the speckle-related modulus depends on the statistical model of the wavelet coefficients. Several models have been proposed for characterizing speckle, including the mixture Gaussian distribution [12] for the uncompressed speckle image, and the normal inverse Gaussian distribution [23] for the logarithmic compressed speckle image. Except for the Gaussian distribution, most models are analytically too complicated to yield a practical model for the normalized wavelet modulus. To simplify the estimation, we assume that both of speckle-related and edge-related normalized wavelet coefficients are Gaussian distributed. Consequently, the speckle-related normalized modulus $\tilde{M}_j f$ can be modeled by the Rayleigh distribution

$$p(x|\text{noise}) = \frac{x}{\sigma_n^2} \exp\left(-\frac{x^2}{2\sigma_n^2}\right) \quad (33)$$

where x denotes the Rayleigh random variable, σ_n is the standard deviation of the normalized wavelet coefficients. Similarly, $p(x|edge)$ for edge-related $\tilde{M}_j f$ has the same form as (33) with the edge-related standard deviation σ_e. Overall, the normalized wavelet modulus $\tilde{M}_j f$ is given by the Rayleigh mixture model

$$p(x) = \omega_n p(x|noise) + (1 - \omega_n)p(x|edge). \quad (34)$$

We demonstrate the performance of the Rayleigh mixture model in matching the distribution of normalized modulus for both envelop-detected and log-compressed ultrasonic images. As shown in Fig. 2, the envelope-detected image [Fig. 2(a)] is simulated by (27) (see Section IV for details), whereas Fig. 2(b)
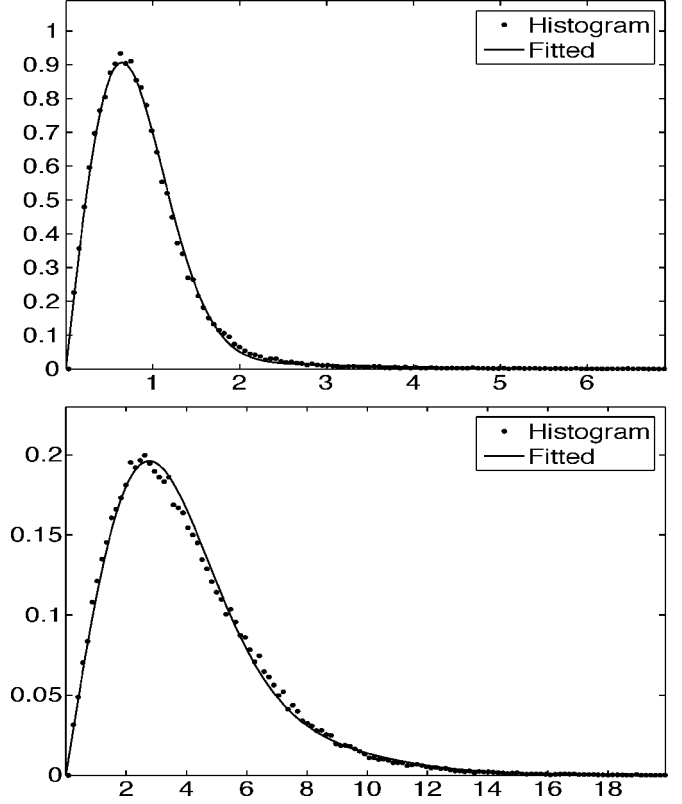

Fig. 3. Histograms and the Rayleigh mixture model fitting of the normalized modulus at scale 2^2 for the simulated envelope-detected speckle image (top) and real echocardiographic image (bottom), shown in Fig. 2(a),(b), respectively.

is a real echocardiographic image (four chamber view). Both of images are decomposed by MZ-DWT. The histograms of normalized modulus and their corresponding Rayleigh mixture fitting at the resolution of 2^2 are shown in Fig. 3. The results indicate that the Rayleigh mixture model can well characterize the statistics of the normalized wavelet modulus for both envelop-detected and log-compressed ultrasonic images.

C. Diffusion Threshold

1) Estimation Based on the Homogenous Speckle Region: The diffusion threshold should reflect the noise variation in the multiscale wavelet modulus. The traditional threshold estimation, such as using a constant value or histogram-based estimation (90% integral of histogram, suggested in [5]), is usually difficult to control in producing a satisfactory result. Extended from the concept of C_u in the spatial case, the diffusion threshold can be estimated by the noise variation present in the homogenous speckle region of the image. This has been pointed out by Yu and Acton [8]. However, due to the difficulty of automatic selection of a homogenous region, they simplified the threshold estimation by using a constant with the predesigned exponential decay function. Such an estimation becomes less flexible with a more complicated image.

We pursue the concept of threshold estimation based on the homogenous region. First, we study the relationship between the estimated threshold and the resolution scales, using a manual selection method. When the image is decomposed into multiscale, the modulus in the coarser scale $(j \geq 2)$ tends to be much
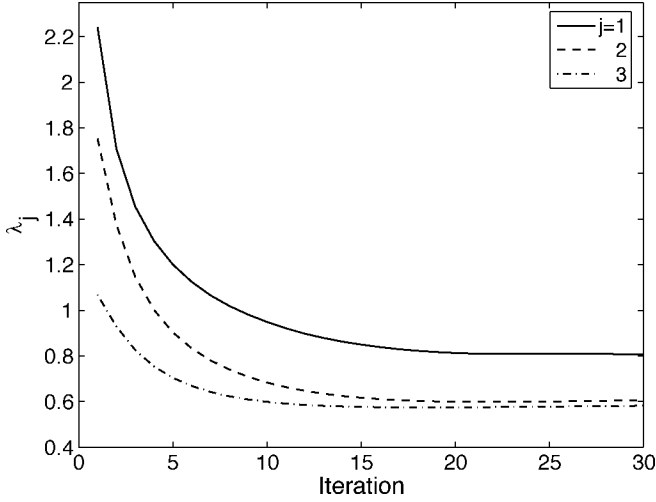
Fig. 4. Diffusion thresholds λ_j ($j = 1, 2, 3$) estimated from the homogenous region in Fig. 2(b).

smoother than that for the finer scale. Therefore, we reduce the threshold of coarser scale to encourage edge preservation. The homogenous-region based threshold for the multiscale wavelet diffusion is proposed as

$$\lambda_j = \frac{\tilde{M}_j f_u}{\sqrt{2}^{j'}} \qquad (35)$$

where $\tilde{M}_j f_u$ represents the mean normalized modulus for the homogenous region u, and j' is the scale factor. Empirically, we use $j' = 0$ for $j = 1$ and $j' = j$ for $j \geq 2$.

In our experiments, the proposed threshold estimator performs well for various speckle images with different noise levels. As an example, Fig. 4 shows an homogenous-region estimated threshold λ_j, which is estimated by the manually selected homogenous region (e.g., cavity of right ventricle) of Fig. 2(b). With this threshold, we are able to generate a result similar to the one shown in Fig. 10(d). After removal of the signal mean, the noise-related $\tilde{M}_j f$ in the homogenous region can generally represent the intrinsic noise level for the whole image. With iterative diffusion, the noise, which is originally Rayleigh distributed, gradually becomes Gaussian distributed. As shown in Fig. 4, the estimated threshold decays quickly from a large initial value to a small constant. Therefore, such a threshold would resist the boundary oversmoothing associated with the diffusion process. The homogenous region estimation method can be adapted well to complicated speckle images. However, manual selection of the homogenous region is always laborious and unstable for practical application. Hence, a scheme for the automatic determination of homogenous regions within an image would be very desirable.

2) Speckle Image Classification: We use likelihood classification and cross-scale edge consistence to separate the homogenous speckle regions from others. For the classification model, we assume that the image consists with three classes: edges, speckle and background. The background commonly exists in the medical ultrasound image, e.g., the region outside scanning region. Background removal is necessary to reduce the estimation error and increase speed. Due to its constant value,

the background can be easily removed with intensity thresholding. The problem then becomes binary classification: specifically, classification of the edge-related and the speckle-related components in the normalized modulus. From assumption (34), the normalized modulus is modeled as a Rayleigh mixture distribution. We use the expectation-maximization (EM) method [24] to estimate the parameters ω_n, σ_n and σ_e of (34). Typically, the number of noise-related coefficients is much larger than those related to edges, and the peak of the normalized modulus histogram is most likely due to noise-related coefficients. Therefore, the initial value of σ_n is estimated by the regression method, $\sigma_n = \sqrt{\pi/2} \max(h_i)$, where h_i is the segment of histogram. Involved computation is reduced with such initialization. With the estimated parameters, the image is segmented by likelihood classification [25], and the classification threshold is given by

$$T = \sqrt{\frac{2\left(\log\frac{\sigma_n^2}{\sigma_e^2} + \frac{\omega_n}{1-\omega_n}\right)}{\left|\frac{1}{\sigma_e^2} - \frac{1}{\sigma_n^2}\right|}}. \qquad (36)$$

To achieve a stable classification, we rely on the persistence of the edge-related normalized modulus across resolution scale. In particular, for an image with background removed, a coarse-to-fine classification method [3] can be used to determine the homogenous region U_j

$$U_j = \begin{cases} 1, & \left[(1 - U_{j+1})\tilde{M}_{j+1}f\right]\tilde{M}_j f < K^2 T_j T_{j+1} \\ 0, & \text{elsewhere} \end{cases}. \qquad (37)$$

Here, K is a tunable parameter that controls the region of interest, and $(1 - U_{j+1})\tilde{M}_{j+1}f$ represents the edge-related components of normalized modulus at scale $j+1$. For coarsest scale, we assume $\tilde{M}_J f$ contains only edges of the image, with $U_J = 0$. In Fig. 5, we demonstrate the performance of the coarse-to-fine classification for the two test images (Fig. 2). For both test images, $K = 1$, and the classified homogenous speckle-related $\tilde{M}_j f$ at different resolutions are shown in white. It is clearly shown that the identified speckle-related components decrease with an increase in decomposition level, whereas edge-related components increase.

With the detected homogenous regions at different scales, the diffusion threshold is computed as

$$\lambda_j = \frac{\text{Mean}(U_j \tilde{M}_j f)}{\sqrt{2}^{j'}}. \qquad (38)$$

From (37) and (38), the parameter K of (38) plays a tuning role in determining the diffusion threshold, and further controls the denoising result. When $K = 0$, all coefficients are related to edges. Consequently, $\lambda_j = 0$, and no filtering needs to be performed. When K is extremely large, all coefficients are related to noise. As a consequence, λ_j is proportional to the mean of normalized modulus. In general, when K increases, more coefficients close to edges are contributed to the threshold calculation. Since these coefficients generally have large values, a large value of K would lead to a large diffusion threshold. On another hand, a small value of K leads to a small threshold. Later in Section IV, we further study the influence of K in controlling the diffusion performance. Briefly, we show that a reasonable value of K always produces a stable performance improvement
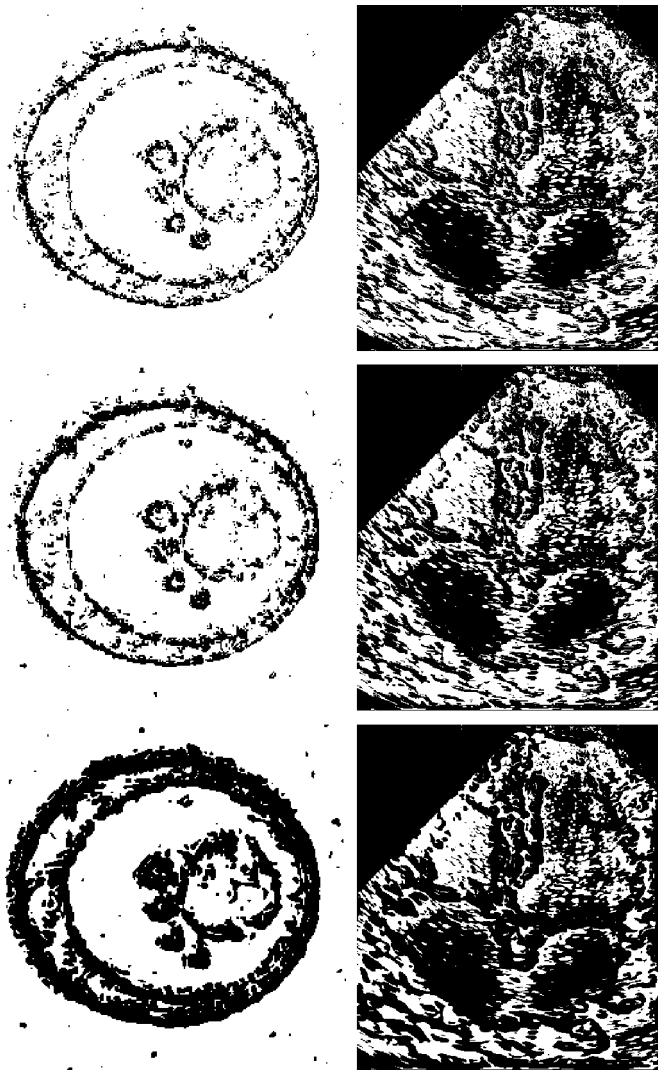
Fig. 5. Classified homogenous speckle regions (white) at scale 2^1, 2^2, 2^3 (from top to bottom) for the simulated envelop-detected speckle image (left column) and real echocardiographic image (right column).

with iteration. In fact, the selection of K is determined by the particular application. As an example of a low-speckle image, ultrasonic brain imaging requires tiny structure detection. Consequently, a small value (e.g., $K = 0.5$) can produce a satisfactory despeckling result without destroying weak edges. On another hand, for large boundary detection, such as the cardiac structure in echocardiographic image, a large value of K (e.g., $K = 2$) will reduce most speckle and eliminate the texture of objects. This can reduce the computational cost and improve the accuracy of a segmentation method.

In summary, we generalize our algorithm as the following.

1) Decompose the noisy image $f(x, y)$ into $S_j f$ and $W_j^d f$ by 2-D MZ-DWT.
2) Compute the normalized modulus $\tilde{M}_j f$ using (29) or (32) according to the image type.
3) For a background removed image, estimate the Rayleigh mixture parameters using EM-estimator, and compute the likelihood classification threshold using (36) for each scale.

4) Determine the homogenous region using coarse-to-fine classification rule (37).
5) Compute the diffusion threshold with (38).
6) Compute the wavelet diffusion coefficient $p(\tilde{M}_j f)$ using (23) with a selected diffusivity function.
7) Regularize wavelet coefficients $W_j^d f$ using (24).
8) Reconstruct the image by taking the inverse 2-D MZ-DWT.

The homogenous region classification (steps 3 and 4) is performed on the initial iteration. As part of an iterative filtering algorithm, the other steps are repeated until a desired result is produced.

IV. EXPERIMENTS AND RESULTS

We tested our proposed normalized modulus-based NMWD speckle suppression algorithm on both of the synthetic and real ultrasonic images. With the synthetic envelope-detected and log-compressed images, despeckling performance in terms of image quality indices is compared with other established despeckling methods. With real ultrasonic images, performance improvement is demonstrated for both visualization and segmentation purposes. In our experiments, the Weickert filter [6] was used as the diffusivity function $g(\eta)$ in (23) for its robustness regarding boundary preservation

$$g(\eta) = \begin{cases} 1, & \eta \leq 0 \\ 1 - \exp\left[\frac{-3.315}{\left(\frac{\eta}{\lambda}\right)^4}\right], & \eta > 0 \end{cases} . \qquad (39)$$

A suitable choice for the smoothing function $\theta(x, y)$ in (5) was a cubic spline with compact support [15]. Therefore, in our implementation, quadratic spline wavelet filters were used for decomposition and reconstruction. A three-level NMWD is employed on all test images (see Fig. 1).

A. Denoising Results for the Simulated Image

To quantitatively evaluate the despeckling performance of the proposed algorithm, we first experimented with the synthetic speckle images. We generated spatial correlated speckle noise by lowpass filtering a complex Gaussian random field and taking the magnitude of the filtered output [3], [26], [27]. To better mimic the appearance of the real image, we controlled the correlation length of speckle by appropriately setting the size of the kernel. The ground truth image [Fig. 6(a)] was constructed by using seven elliptic targets with different intensities on a dark background. As shown in Fig. 2(a), the envelope-detected ultrasound image was simulated by corrupting the ground truth image with full speckle noise using (27). For the log-compressed image, the noise was generated so as to have both the appearance of speckle and the norm distribution. The image was simulated using (30), and the result is shown in Fig. 7(a).

We compared the performance of our speckle suppression algorithm with that of other speckle reduction techniques: namely, the speckle reducing anisotropic diffusion (SRAD) technique [8], and the wavelet generalized likelihood ratio filtering method (GenLik) [3]. Although both algorithms are designed to reduce speckle and preserve the edges of objects, the differences are: 1) SRAD emphasizes edge-enhancement more than visualization improvement, whereas GenLik focuses to a greater extent
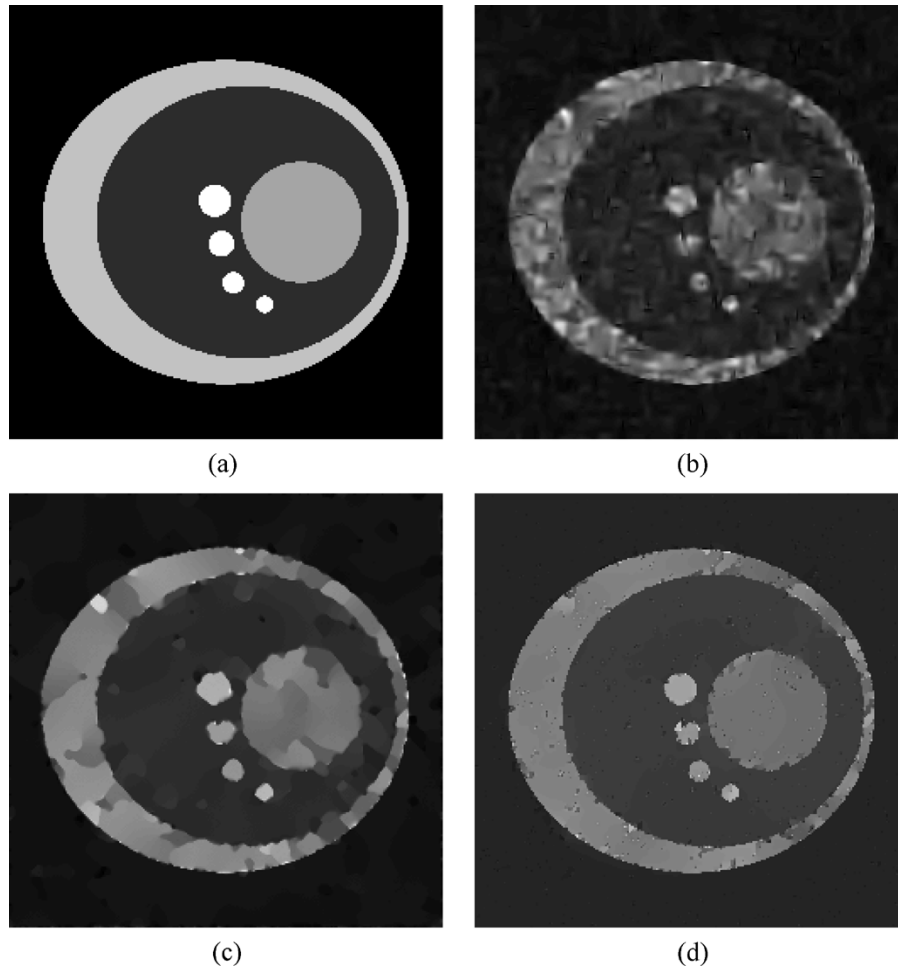
Fig. 6. Denoising results for the simulated envelope-detected ultrasonic image [Fig. 2(a)]. (a) Echogeneity map. Results filtered by (b) GenLik, (c) SRAD, and (d) NMWD, respectively.

on visualization improvement. 2) SRAD is a nonlinear diffusion based method, whereas GenLik is a multiscale wavelet denoising method. 3) SRAD takes the envelope-detected image as its input, whereas GenLik prefers the log-compressed image. In addition, Yu and Acton [8] have demonstrated the performance superiority of SRAD over Perona–Malik nonlinear diffusion, the Lee and Frost filters; whereas Pizuriaca *et al.* [3] have shown that GenLik outperforms the homomorphic Wiener filter. Thus, we consider that a performance comparison between our algorithm and these two despeckling filters, represents an adequate demonstration that the proposed algorithm fulfills the denoising design requirements.

A first comparison was made using the envelope-detected full speckle image [Fig. 2(a)]. In SRAD implementation, q_0 in (26) is reduced exponentially with iteration, such as with $q_0(t) = q_0(0)\exp(-t/6)$. Here, $q_0(0)$ equals to $\sqrt{1/L}$ for intensity images and $\sqrt{(4/\pi - 1)/L}$ for amplitude images, and L is the look number. Therefore, for the envelope detected ultrasound image, we used $q_0(0) = 0.5227$ ($L = 1$) in the test. The time step was set as $\triangle t = 0.05$, and the number of iterations was 300. The diffusivity function was chosen as (26), and the result is shown in Fig. 6(c). The GenLik method was evaluated using the original implementation, which is available in the author's website (http://telin.rug.ac.be/~sanja/). For best performance, the test image was first log-transformed prior to being

filtered by the GenLik method. The filtered result was recovered by the exponential function. The edge-detection threshold factor was chosen as 5 with a window size 5×5, and the result is shown in Fig. 6(b). In our algorithm, the parameter K in (37) was set to 3. The window size for estimation of the mean is 3×3 at the first scale. The image was processed with 30 iterations, and the output is shown in Fig. 6(d).

We further compared the denoising performance of all three filters on the synthetic log-compressed image [Fig. 7(a)]. Since SRAD takes an envelope-detected image as input, the test image was first decompressed by taking the exponential of the image divided by a compression coefficient prior to being processed by SRAD. The compression coefficient, D, is estimated empirically to achieve the best performance. Specifically, $D = 50$ for this test image. The other parameters were the same as those used in the first experiment. For the GenLik method, the test image was directly used as the input. The edge-detection threshold factor was chosen as 5 with window size 5×5. In our algorithm, the parameter K was set to 2, the despeckling process ran adaptively with 30 iterations. The denoised images recovered by the GenLik, SRAD and proposed algorithm are shown in Fig. 7(b)–(d).

Since speckle in the ultrasound image is modeled as the multiplicative noise, a linear image fidelity criterion, such as MSE or SNR, is not always an accurate measure of speckle suppres-
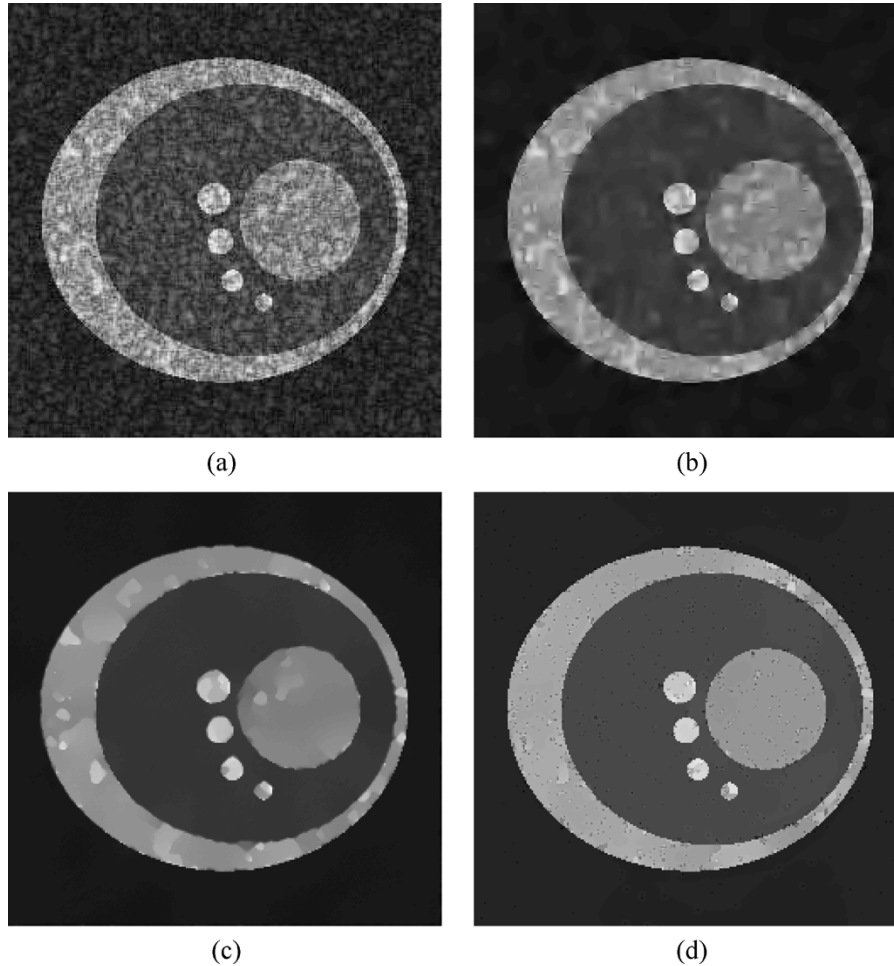
Fig. 7.   Denoising results for the simulated log-compressed ultrasonic image. (a) Original image. Results filtered by (b) GenLik, (c) SRAD, and (d) NMWD, respectively.

sion in images. In our studies, the denoising algorithm performance is quantified by using two quality indices: a noisy suppression quality index ρ [26], [28], an edge preservation index, called figure of merit (FOM) [8], [29]. Speckle suppression is evaluated by comparing the structure similarity between denoised image and noise-free image. A correlation-based structure similarity measure is given by [26], [28]

$$\rho = \frac{\sum\limits_{i,j \in w} (x(i,j) - \mu_x)(y(i,j) - \mu_y)}{\sqrt{\sum\limits_{i,j \in w} (x(i,j) - \mu_x)^2 \cdot \sum\limits_{i,j \in w} (y(i,j) - \mu_y)^2}} \quad (40)$$

where μ_x and μ_y are mean values of interested region w in the noise-free image x and denoised image y, respectively. The FOM is defined as

$$\text{FOM} = \frac{1}{\max(n_d, n_r)} \sum_{i=1}^{n_d} \frac{1}{1 + \gamma d_i^2} \quad (41)$$

where n_d is the number of detected edge pixels in the test noisy image, n_r is the number of reference edge pixels in the noise-free image, d_i is the Euclidean distance between the ith detected edge pixel and the nearest reference edge pixel, and γ is a constant typically set to 0.11. We use the Laplacian of Gaussian method to detect the edges. If the measured image is close to the reference image, the values of ρ and FOM should be close to 1.

TABLE II
PERFORMANCE COMPARISON FOR DIFFERENT DENOISING TECHNIQUES

Method	Speckle Image		Log-Speckle Image	
	ρ	FOM	ρ	FOM
Noisy image	0.7583	0.2281	0.9113	0.2245
GenLik	0.9272	0.4953	0.9741	0.5297
SRAD	0.9533	0.6121	0.9773	0.6661
NMWD	0.9717	0.7566	0.9886	0.9071

The performance quality of two experiments, in terms of ρ and FOM, are listed in Table II. In comparing the denoising results, we found that all of the speckle reduction methods can eliminate speckle in most homogenous regions. However, only the proposed method can significantly reduce speckle in both high and low intensity regions, as well as preserve both high-contrast and low-contrast edges. We also iteratively applied the GenLik method on the test images, however, no significant performance improvement was observed. For example, after the log-compressed image was processed by GenLik for 30 iterations, FOM $= 0.5816$, and $\rho = 0.9776$. This indicates that nonlinear diffusion-based methods have a significant advantage in being able to suppress speckle, while preserving edges.

We also studied the stability of the parameter K in the proposed algorithm. The test images were processed with different value of K, specifically, 0.5, 1.0, 2.0, 3.0, 4.0, and 5.0. For each
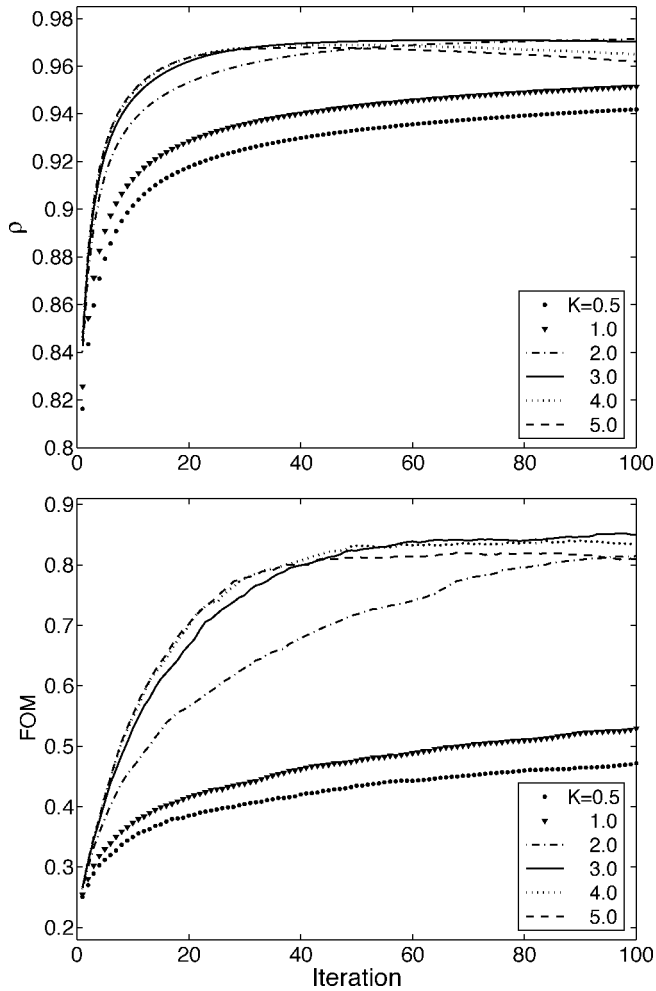
Fig. 8. Image quality indices ρ (top) and FOM (bottom), after the simulated envelope-detected image is filtered by NMWD with different values of K.
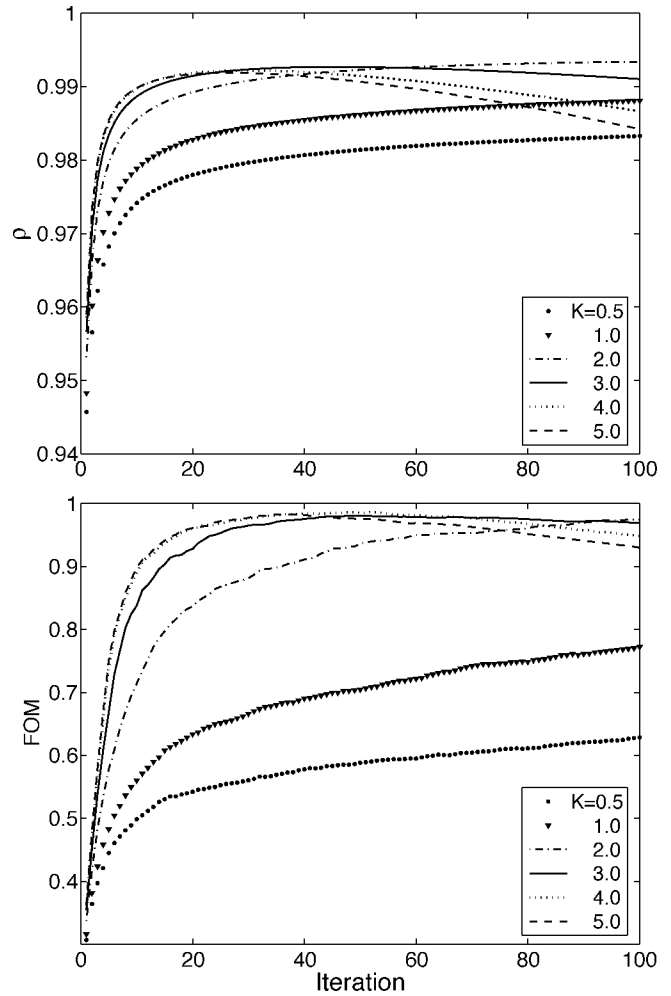

Fig. 9. Image quality indices ρ (top) and FOM (bottom), after the simulated log-compressed image is filtered by NMWD with different values of K.

value, the image was processed with 100 iterations. Figs. 8 and 9 demonstrate the effect of K on controlling the denoising performance of the proposed algorithm. When K is within a threshold, (e.g., $K = 3$ for the enveloped-detected image, $K = 2$ for the log-compressed image), both ρ and FOM do not decrease with iteration. Above this value, however, these quality indices decrease with iteration. Such variation is within expectation. A large value of K indicates more coefficients close to edges are counted in the diffusion threshold estimation. If the diffusion threshold is overestimated, edge smearing occurs, and the quality indices decrease with iteration. This becomes evident, when $K = 5$. In that case, the diffusion threshold is equivalent to the mean of normalized modulus at the current scale. However, for a value below threshold, the role of K always improves the image quality with iteration in a stable fashion. The experiments also illustrate the effect of the number of iterations on performance. For a given value of K, NMWD fast approaches reasonable performance within 20 to 40 iterations. After that, only small improvements are observed. It suggests that diffusion with 20 to 40 iterations has the highest computational efficiency.

The computational complexity of proposed algorithm can be analyzed from two stand points: the main procedures (excluding EM estimation) and the EM algorithm. Given N

pixels, the complexity of EM estimation for two-Rayleigh mixture is $\mathcal{O}(i \times N)$, where i is the iteration number. In the main procedures, wavelet decomposition and reconstruction exhibit the largest complexity, $\mathcal{O}(N \log N)$. Overall, the computational complexity of the complete algorithm is $\mathcal{O}(i \times N + j \times N \log N)$, where j is the iteration number of wavelet diffusion. In practice, NMWD was implemented in Matlab (Mathworks, Natick, MA), where the main procedures achieved a processing rate of 0.19 s/scale/iteration for a 256×256 image on a PC with a Pentium 4 (2.4 GHz) processor.

B. Real Image

In the first *in vivo* image experiment, we examined the image quality improvement of the proposed algorithm for both visualization and auto-segmentation. Fig. 10(a) [also Fig. 2(b)] shows an echocardiographic image of the human heart, in four-chamber view. The data was acquired using a HDI5000 ultrasound scanner manufactured by ATL, a Philips Medical Systems Company. Two experiments with two different values of K were performed on the test image. Specifically, a small value of $K = 0.5$ was used to test visualization improvement, whereas a large value $K = 1.5$ was used for segmentation improvement. The wavelet diffusion was performed for 30 iterations for both experiments, and the denoising results are
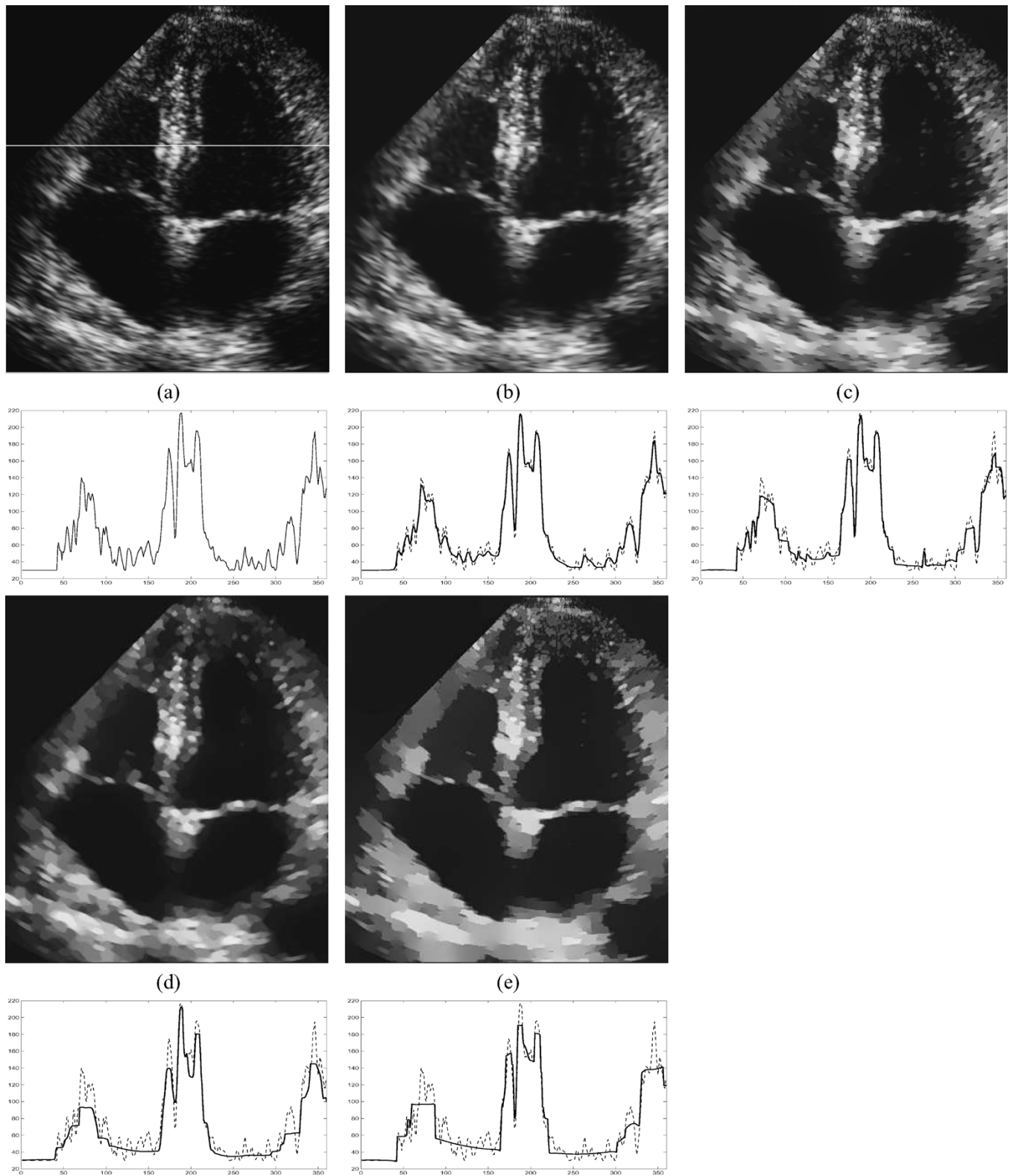
Fig. 10. Denoising results for the echocardiographic image. (a) Original image. Results filtered by (b) the GenLik method, (c) NMWD ($K = 0.5$), (d) SRAD, and (e) NMWD ($K = 1.5$), respectively. The profiles along the highlight line of the original image (a) are shown in their following row.

shown in Fig. 10(c),(e). For clear illustration, the profiles, along the highlight line in the original image, are also compared. The test image was also filtered by two subject algorithms. We used the GenLik method for the comparison on visualization im-provement. The edge-detection threshold factor of GenLik

was chosen as 5 with window size 5×5. To examine the visual improvements, we focused on speckle reduction within the cavity and at the wall of right ventricle (indicated by the highlight line). We also focused on structure enhancement at the moderator band near the apex of the right ventricle. As
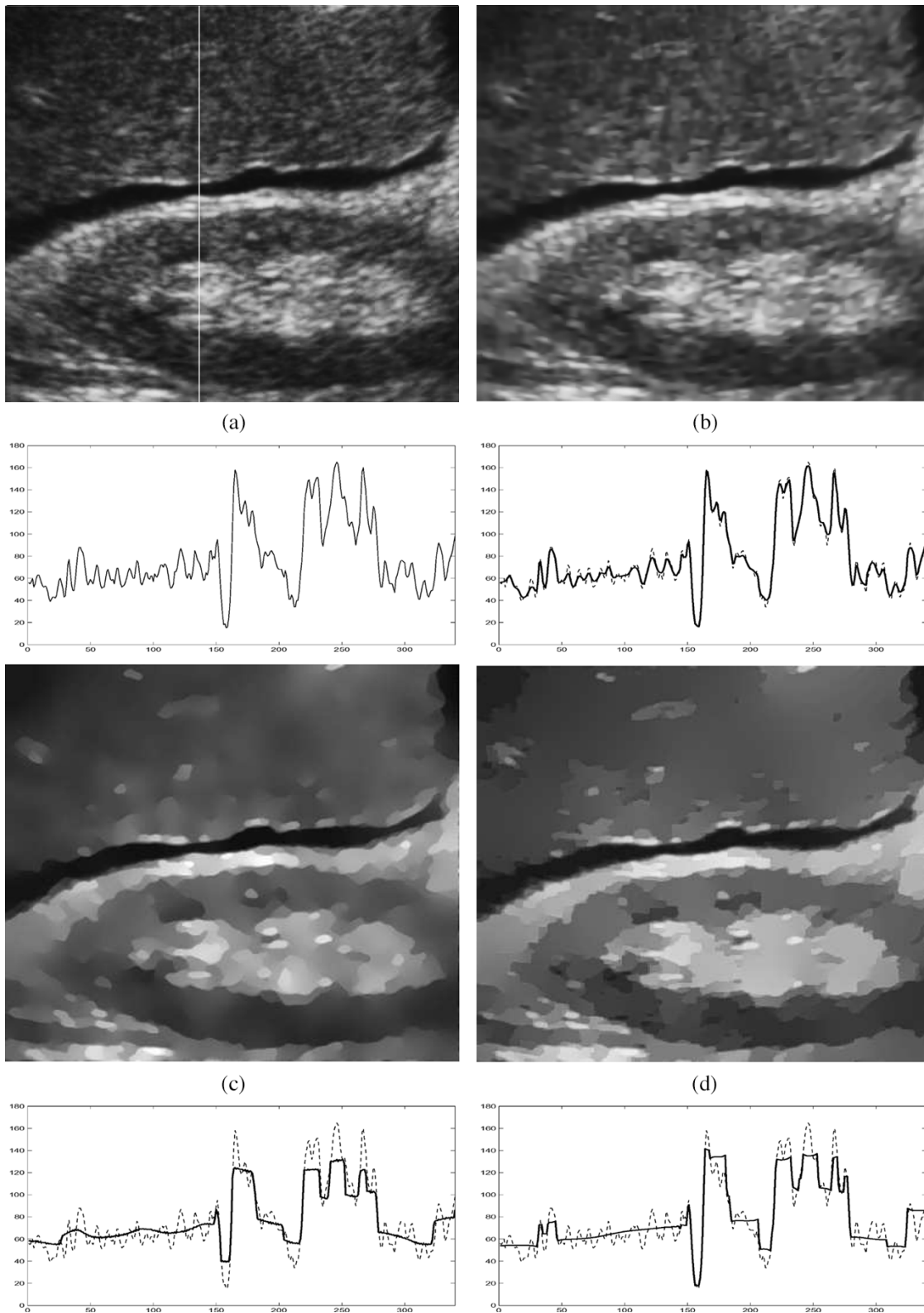
Fig. 11.   Denoising results for a liver image. (a) Original image. Results filtered by (b) the GenLik method, (c) SRAD, and (d) NMWD, respectively. The profiles along the highlight line of the original image (a) are shown in their following row.

indicated by the profiles, our algorithm produces a better result for the purpose of visualization. For the segmentation-purposed comparison, we used SRAD for its edge enhancement feature. Specifically, the compression coefficient $D = 35$ was used, and the other parameters were identical to those used in the previous

experiment. In this case, we compared speckle suppression and texture removal in the wall region, and the structure enhancement of all ventricular walls. Comparing Fig. 10(d) and (e), we found that the proposed algorithm achieved better speckle removal and edge enhancement than the SRAD method.

For a real ultrasound image, criterion used in evaluating the denoising result may be quite subjective to the specific objectives of the observers. Consequently, the proposed algorithm has to be flexible so that it can be readily adapted to the requirements of different applications. With a small value of K, the proposed algorithm can preserve the textured region, as well as the formation of uniform area in the filtered image. In the sense of visualization improvement, such a filtered result would be visually favored in clinical diagnosis. However, for auto-segmentation applications, the very same result may cause the active contour to be trapped by the retained textured region and granular boundaries. To improve auto-segmentation, we recommend using a large value of K, so as to remove speckle texture in the homogenous region and enhance the edges of structure.

In general, for a nonlinear diffusion method, the balance between noise suppression and edge preservation often makes threshold selection difficult. A large diffusion threshold often leads to the significant tiny structure smearing with noise, whereas a small threshold will produce unsatisfactory noise suppression for boundary tracking. In the next example, we demonstrate that the algorithm can achieve speckle suppression and tiny structure preservation simultaneously. The test image is an ultrasound scan of human liver and kidney region [Fig. 11(a)], which is obtained from public medical image database, MedPix (http://rad.usuhs.mil/medpix/medpix.html). In this test, we focus on evaluating speckle removal in the uniform region of the liver, and the edge enhancement of the nodular structure of the liver parenchyma. The denoised results are shown in Fig. 11(b)–(d). These results were also compared via the profiles, along the highlight line in the original image. As the results show, the proposed algorithm outperforms the other two filters by clearly outlining the noduli on the liver surface, while suppressing most of speckle in the liver and kidney regions. Our result [Fig. 11(d)] suggests that the proposed method could lead to reliable and efficient nodule detection in the diagnosis of cirrhosis of the liver.

V. CONCLUSION

This paper introduces a novel multiscale normalized modulus-based wavelet diffusion method for speckle suppression and edge enhancement in ultrasound images. In our approach, speckle image is iteratively filtered by the nonlinear diffusivity function via the framework of the dyadic wavelet transform. In each iteration, the noisy image is processed with three-step wavelet shrinkage-like procedures: decomposition, regularization and reconstruction. Considering the statistical behavior of speckle, successful employment of nonlinear wavelet diffusion in a speckle suppression task, requires three appropriately designed components: an edge detector, a diffusion threshold and a diffusivity function. Since most diffusivity functions developed from spatial nonlinear diffusion have been shown to satisfy the denoising requirement, our work mainly focuses on the design of the first two components above. We use the normalized wavelet modulus as the edge detector to characterize the intrinsic signal/noise variation. The significant feature provided by this edge detector is its versatility for images of different

types. Thus, our algorithm can deal directly with either envelope-detected speckle image or log-compressed medical ultrasonic image without any pretransform. To adapt the noise variation with iteration, the diffusion threshold is estimated from the normalized modulus in the homogenous speckle regions. The automatic identification of homogenous regions is implemented using a two-stage classification. First, the normalized modulus at each scale is classified using the likelihood method based on the Rayleigh mixture model. Second, the homogenous speckle region is identified by a coarse-to-fine classification utilizing the edge persistence across scale. In this procedure, a tuning parameter (K) is introduced to adjust the diffusion threshold, and it further controls the final denoising result. Relying on this feature, the proposed algorithm is highly flexible in producing a desired result for a specific application.

Using synthetic envelope-detected images, we have shown that the proposed algorithm is a versatile speckle reduction technique for both envelope-detected and log-compressed speckle images. We also have demonstrated the performance superiority of the proposed algorithm over the SRAD and GenLik methods in terms of speckle suppression and edge preservation indices. With real ultrasonic images, we have shown that the proposed algorithm is quite robust in producing a desired result either for visualization enhancement or for auto-segmentation improvement. In summary, by combining the sparsity and multi-resolution properties of wavelets, with the edge preservation and enhancement features of the nonlinear diffusion, our algorithm provides very significant speckle suppression and edge enhancement for the purposes of visualization and automatic structure detection.

REFERENCES

[1] J. S. Lee, "Digital image enhancement and noise filtering by use of local statistics," *IEEE Trans. Pattern Anal. Mach. Intell.*, vol. PAMI-2, pp. 165–168, Mar. 1980.

[2] X. Zong, A. F. Laine, and E. A. Geiser, "Speckle reduction and contrast enhancement of echocardiograms via multiscale nonlinear processing," *IEEE Trans. Med. Imag.*, vol. 17, no. 8, pp. 532–540, Aug. 1998.

[3] A. Pizuriaca, W. Philips, I. Lemahieu, and M. Acheroy, "A versatile wavelet domain noise filtration technique for medical imaging," *IEEE Trans. Med. Imag.*, vol. 22, no. 3, pp. 323–331, Mar. 2003.

[4] D. Mumford and J. Shah, "Optimal approximations by piecewise smooth functions and associated variational problems," *Commun. Pure Appl. Math.*, vol. 42, pp. 577–684, 1989.

[5] P. Perona and J. Malik, "Scale-space and edge detection using anisotropic diffusion," *IEEE Trans. Pattern Anal. Mach. Intell.*, vol. 12, no. 7, pp. 629–639, Jul. 1990.

[6] J. Weickert, *Anisotropic Diffusion in Image Processing*. Stuttgart, Germany: Teubner, 1998.

[7] L. I. Rudin, S. Osher, and E. Fatemi, "Nonlinear total variation based noiseremoval algorithms," *Physica D*, vol. 20, pp. 259–268, 1992.

[8] Y. Yu and S. T. Acton, "Speckle reducing anisotropic diffusion," *IEEE Trans. Image Process.*, vol. 11, no. 11, pp. 1260–1270, Nov. 2002.

[9] V. S. Frost, K. Shanmugan, and J. Holtzman, "A model for radar images and its applications to adaptive digital filtering of multiplicative noise," *IEEE Trans. Pattern Anal. Mach. Intell.*, vol. PAMI-4, pp. 157–165, 1982.

[10] S. Foucher, G. Bénié, and J.-M. Boucher, "Multiscale map filtering of SAR images," *IEEE Trans. Image Process.*, vol. 10, no. 1, pp. 49–60, Jan. 2001.

[11] F. Argenti and L. Alparone, "Speckle removal from SAR images in the undecimated wavelet domain," *IEEE Trans. Geosci. Remote Sens.*, vol. 40, no. 11, pp. 2363–2374, Nov. 2002.

[12] M. Dia, C. Peng, A. K. Chan, and D. Loguinov, "Bayesian wavelet shrinkage with edge detection for SAR image despeckling," *IEEE Trans. Geosci. Remote Sens.*, vol. 42, no. 8, pp. 1642–1648, Aug. 2004.

[13] A. C. Shih, H. M. Liao, and C. Lu, "A new iterated two-band diffusion equation: theory and its application," *IEEE Trans. Image Process.*, vol. 12, no. 4, pp. 466–476, Apr. 2003.

[14] J. S. Jin, Y. Wang, and J. Hiller, "An adaptive nonlinear diffusion algorithm for filtering medical images," *IEEE Trans. Inf. Technol. Biomed.*, vol. 4, no. 12, pp. 298–305, Dec. 2000.

[15] S. Mallat and S. Zhong, "Characterization of signals from multiscale edges," *IEEE Trans. Pattern Anal. Mach. Intell.*, vol. 14, no. 7, pp. 710–732, Jul. 1992.

[16] N. F. Law and W. C. Siu, "An efficient computational scheme for the two-dimensional overcomplete wavelet transform," *IEEE Trans. Signal Process.*, vol. 50, no. 11, pp. 2806–2819, Nov. 2002.

[17] P. Mrázek, J. Weickert, and G. Steidl, *Lecture Notes in Computer Science*, L. D. Griffin Steidl and M.Lillholm Steidl, Eds. Berlin, Germany: Springer-Verlag, 2003, vol. 2695, Correspondences Between Wavelet Shrinkage and Nonlinear Diffusion. Scale-Space, pp. 101–116.

[18] J. Weickert, "A review of nonlinear diffusion filtering," in *Lecture Notes in Computer Science*. Berlin, Germany: Springer-Verlag, 1997, vol. 1252, Scale-Space Theory in Computer Vision, pp. 3–28.

[19] D. L. Donoho and I. M. Johnstone, "Ideal spatial adaptation by wavelet shrinkage," *Biometrika*, vol. 81, no. 3, pp. 425–455, 1994.

[20] M. Simard, G. DeGrandi, K. P. B. Thomson, and G. B. Benie, "Analysis of speckle noise contribution on wavelet decomposition of SAR images," *IEEE Trans. Geosci. Remote Sens.*, vol. 36, no. 11, pp. 1953–1962, Nov. 1998.

[21] V. Dutt and J. Greenleaf, "Adaptive speckle reduction filter for log-compressed b-scan images," *IEEE Trans. Med. Imag.*, vol. 15, no. 6, pp. 802–813, Dec. 1996.

[22] A. Lopes, R. Touzi, and E. Nezry, "Adaptive speckle filters and scene heterogeneity," *IEEE Trans. Geosci. Remote Sens.*, vol. 28, no. 6, pp. 992–1000, Jun. 1990.

[23] S. Solbø and T. Eltoft, "Homomorphic wavelet-based statistical despeckling of SAR images," *IEEE Trans. Geosci. Remote Sens.*, vol. 42, no. 4, pp. 711–721, Apr. 2004.

[24] A. Dempster, N. Laird, and D. Rubin, "Maximum likelihood from incomplete data via the EM algorithm," *J. Roy. Statist. Soc.*, ser. B, vol. 39, no. 1, pp. 1–38, 1977.

[25] K. V. Mardia and T. J. Hainsworth, "A spatial thresholding method for image segmentation," *IEEE Trans. Pattern Anal. Mach. Intell.*, vol. 10, no. 11, pp. 919–927, Nov. 1988.

[26] F. Sattar, L. Floreby, G. Salomonsson, and B. Lovstrom, "Image enhancement based on a nonlinear multiscale method," *IEEE Trans. Image Process.*, vol. 6, no. 6, pp. 888–895, Jun. 1997.

[27] A. Achim, A. Bezerianos, and P. Tsakalides, "Novel Bayesian multiscale methods for speckle removal in medical ultrasound images," *IEEE Trans. Med. Imag.*, vol. 20, no. 8, pp. 772–783, Aug. 2001.

[28] Z. Wang, A. C. Bovik, H. R. Sheikh, and E. P. Simoncelli, "Image quality assessment: from error visibility to structural similarity," *IEEE Trans. Image Process.*, vol. 13, no. 4, pp. 600–612, Apr. 2004.

[29] W. K. Pratt, *Digital Image Processing*. New York: Wiley, 1977.